**Title**

High-Temporal-Resolution Kinetic Modeling of Lung Tumors with Dual-Blood Input Function Using Total-Body Dynamic PET.

**Permalink**

**Journal**

**Authors**

Wang, Yiran

Abdelhafez, Yasser

Spencer, Benjamin

et al.

**Publication Date**

**DOI**

# High-Temporal-Resolution Kinetic Modeling of Lung Tumors with Dual-Blood Input Function Using Total-Body Dynamic PET

Yiran Wang[1,2], Yasser G. Abdelhafez[1,3], Benjamin A. Spencer[1], Rashmi Verma[4], Mamta Parikh[4], Nicholas Stollenwerk[4], Lorenzo Nardo[1], Terry Jones[1], Ramsey D. Badawi[1,2], Simon R. Cherry[1,2], and Guobao Wang[1]

[1]*Department of Radiology, University of California Davis Medical Center, Sacramento, California;* [2]*Department of Biomedical Engineering, University of California, Davis, Davis, California;* [3]*Nuclear Medicine Unit, South Egypt Cancer Institute, Assiut University, Assiut, Egypt; and* [4]*Comprehensive Cancer Center, University of California Davis Medical Center, Sacramento, California*

The lungs are supplied by both the pulmonary arteries carrying deoxygenated blood originating from the right ventricle and the bronchial arteries carrying oxygenated blood downstream from the left ventricle. However, this effect of dual blood supply has never been investigated using PET, partially because the temporal resolution of conventional dynamic PET scans is limited. The advent of PET scanners with a long axial field of view, such as the uEXPLORER total-body PET/CT system, permits dynamic imaging with high temporal resolution (HTR). In this work, we modeled the dual-blood input function (DBIF) and studied its impact on the kinetic quantification of normal lung tissue and lung tumors using HTR dynamic PET imaging. **Methods:** Thirteen healthy subjects and 6 cancer subjects with lung tumors underwent a dynamic $^{18}$F-FDG scan with the uEXPLORER for 1 h. Data were reconstructed into dynamic frames of 1 s in the early phase. Regional time–activity curves of lung tissue and tumors were analyzed using a 2-tissue compartmental model with 3 different input functions: the right ventricle input function, left ventricle input function, and proposed DBIF, all with time delay and dispersion corrections. These models were compared for time–activity curve fitting quality using the corrected Akaike information criterion and for differentiating lung tumors from lung tissue using the Mann–Whitney $U$ test. Voxelwise multiparametric images by the DBIF model were further generated to verify the regional kinetic analysis. **Results:** The effect of dual blood supply was pronounced in the high-temporal-resolution time–activity curves of lung tumors. The DBIF model achieved better time–activity curve fitting than the other 2 single-input models according to the corrected Akaike information criterion. The estimated fraction of left ventricle input was low in normal lung tissue of healthy subjects but much higher in lung tumors ($\sim$0.04 vs. $\sim$0.3, $P < 0.0003$). The DBIF model also showed better robustness in the difference in $^{18}$F-FDG net influx rate $K_i$ and delivery rate $K_1$ between lung tumors and normal lung tissue. Multiparametric imaging with the DBIF model further confirmed the differences in tracer kinetics between normal lung tissue and lung tumors. **Conclusion:** The effect of dual blood supply in the lungs was demonstrated using HTR dynamic imaging and compartmental modeling with the proposed DBIF model. The effect was small in lung tissue but nonnegligible in lung tumors. HTR dynamic imaging with total-body PET can offer a sensitive tool for investigating lung diseases.

**Key Words:** total-body dynamic PET; lung cancer; high temporal resolution; kinetic modeling; dual-blood input function

The lungs have 2 blood supplies: the pulmonary arteries that carry deoxygenated blood originating from the right ventricle (RV) (*1,2*) and the bronchial arteries that carry oxygenated blood downstream from the left ventricle (LV) (*3–5*). Although the blood supply to normal lung tissue is usually dominated by the pulmonary arteries, lung tumors tend to have an increased blood supply fraction from the bronchial arteries (*6–8*). This dual-blood-supply effect of lung tumors has been studied with dynamic CT imaging (*8–11*), though with a limited axial field of view. However, to our best knowledge, it has never been investigated by dynamic PET, partially because the temporal resolution of conventional dynamic PET imaging (*12–14*) has been limited (5–30 s/frame) and not able to detect the rapidly changing early dynamics of the lungs and differentiate the dual blood supplies. As a result, existing lung kinetic modeling approaches for dynamic PET often neglect the effect of dual blood supply and only use a single input function for kinetic modeling (*13,15–17*).

Total-body and long-axial-field-of-view PET scanners (*18–20*) greatly improve the detection sensitivity and hence permit high-temporal-resolution (HTR) dynamic imaging, opening the door for HTR kinetic modeling for the lungs. For example, the uEXPLORER (United Imaging Healthcare) total-body PET/CT scanner allows HTR dynamic PET imaging with 1 s or less per frame (*21–23*). In this study, we exploited the ability of the uEXPLORER for HTR dynamic PET imaging to model the dual-blood input function (DBIF) in the lungs and investigated its impact on the kinetic quantification of normal lung tissue and lung tumors. Modeling of the DBIF may provide useful insights into the bronchial circulation and can potentially benefit the characterization of lung nodules, such as to distinguish malignancy from benign lesions after low-dose CT lung cancer screening (*10,24*).

## MATERIALS AND METHODS

### HTR Dynamic Data Acquisition on Total-Body PET

This study included 13 healthy human subjects (mean age ± SD, 49 ± 15 y; weight, 82 ± 18 kg; 6 men, 7 women) and 6 cancer patients with lung tumors, which include 3 primary lung cancer subjects (age, 68 ± 3 y; weight, 78 ± 8 kg; 2 men, 1 women) and 3

genitourinary cancer subjects with lung metastases (age, $64 \pm 10$ y; weight, $79 \pm 10$ kg; 3 men). All subjects provided written informed consent with the approval of the Institutional Review Board at the University of California, Davis. The subjects were scanned on the uEXPLORER total-body PET/CT system (25) with an ultra-low-dose (140 kVp, 5 mAs) or low-dose (140 kVp, 50 mAs) CT scan performed first, followed by a 60-min total-body dynamic $^{18}$F-FDG PET scan with a dose of about 360 MBq (291–390 MBq) through intravenous administration. The acquired list-mode PET data were reconstructed into a total of 120 frames over 60 min, with HTR frames (1–2 s per frame) in the first 2 min: $60 \times 1$ s, $30 \times 2$ s, $6 \times 10$ s, $6 \times 30$ s, $12 \times 120$ s, and $6 \times 300$ s using the vendor-provided ordered-subset expectation maximization algorithm (4 iterations and 20 subsets) with $4 \times 4 \times 4$ mm$^3$ voxels. Regions of interest (ROIs) were placed in the LV cavity and RV cavity for each subject to extract time–activity curves for image-derived input functions, $C_{\text{LV}}(t)$ and $C_{\text{RV}}(t)$, which provide the bronchial blood supply and pulmonary blood supply to the lungs, respectively. Time–activity curves of nontumor lung tissue were extracted for each of the 6 cancer subjects and 13 healthy subjects by averaging 5 lung ROIs for each subject (1 ROI per each lung lobe; Supplemental Fig. 1A provides an illustrative example; supplemental materials are available at http://jnm.snmjournals.org). In total, 8 lung tumors, including 3 primary lung tumors (from each of the 3 primary lung cancer subjects) and 5 lung metastases (3 from 1 genitourinary cancer subject and 2 from each of the other 2 genitourinary cancer subjects) were also identified among the 6 cancer subjects. ROIs for these lung tumors were placed (Supplemental Fig. 1B), and corresponding time–activity curves were extracted.

## Compartmental Modeling

We used a 2-tissue irreversible compartmental model (26,27) to model the $^{18}$F-FDG kinetics in the lungs (Fig. 1A). The model is described by the following set of differential equations:

$$\frac{d}{dt}\begin{bmatrix} C_{\text{f}}(t) \\ C_{\text{m}}(t) \end{bmatrix} = \begin{bmatrix} -k_2 - k_3 & 0 \\ k_3 & 0 \end{bmatrix}\begin{bmatrix} C_{\text{f}}(t) \\ C_{\text{m}}(t) \end{bmatrix} + \begin{bmatrix} K_1 \\ 0 \end{bmatrix}C_{\text{p}}(t), \quad \text{Eq. 1}$$

where $C_{\text{p}}(t)$ is the blood input function, $C_{\text{f}}(t)$ is the concentration of free-state $^{18}$F-FDG in the tissue, and $C_{\text{m}}(t)$ is the phosphorylated $^{18}$F-FDG ($^{18}$F-FDG-6P) in tissue. $K_1$ (mL/min/cm$^3$) and $k_2$ (min$^{-1}$) are the blood-to-tissue and tissue-to-blood $^{18}$F-FDG delivery rate constants, respectively, and $k_3$ (min$^{-1}$) is the rate constant of $^{18}$F-FDG phosphorylation. The irreversible model is based on the assumption of negligible $^{18}$F-FDG-6P



**FIGURE 1.** (A) 2-tissue irreversible model for kinetic modeling of lung dynamic $^{18}$F-FDG PET. (B) Different blood input functions for HTR lung kinetic modeling. Time delay and dispersion corrections are applied to 3 input functions.

dephosphorylation (i.e., the dephosphorylation rate constant $k_4 = 0$). The total $^{18}$F-FDG concentration measured by PET is modeled as a combination of concentrations in the extravascular tissue and in the blood,

$$C_{\text{T}}(t) = (1 - v_{\text{b}})H(t; \kappa) \otimes C_{\text{p}}(t) + v_{\text{b}}C_{\text{wb}}(t), \quad \text{Eq. 2}$$

where $C_{\text{T}}(t)$ is the modeled total concentration, $v_{\text{b}}$ is the blood volume fraction, and $C_{\text{wb}}(t)$ is the whole-blood tracer concentration, which can be approximated by the image-derived input function. $\kappa = [K_1, k_2, k_3]^{\text{T}}$, and $H(t; \kappa)$ is the impulse response function of the 2-tissue irreversible model: $H(t; \kappa) = \frac{K_1}{k_2 + k_3}\left(k_3 + k_2 e^{-(k_2 + k_3)t}\right)$. With this model, all kinetic parameters are jointly estimated using a nonlinear least-square time–activity curve fitting (28):

$$\hat{\theta} = \arg\min_{\theta} \text{WRSS}(\theta), \ \text{WRSS}(\theta) = \sum_{m=1}^{M} w_m[\check{C}_{\text{T}}(t_m) - C_{\text{T}}(t_m)]^2.$$

Eq. 3

$\check{C}_{\text{T}}(t)$ is the real measured $^{18}$F-FDG concentration. $\text{WRSS}(\theta)$ is the weighted residual sum of squares of the time–activity curve fitting. $\theta$ is the collection of unknown parameters in the kinetic model. $M$ is the total number of dynamic frames. $t_m$ and $w_m$ are the time and the weight of the $m$th frame, respectively. A uniform weight was used in this study (28).

## Single-Blood Input Functions

Because the pulmonary input accounts for most of the total blood input to the lung tissue (4), previous studies (13,15–17) commonly used the RV-derived input function (RVIF) (Fig. 1B) for kinetic modeling of lung tissue. In HTR lung kinetic modeling, it also becomes important to include corrections for time delay and dispersion to the image-derived input function (29). Hence, the RVIF model implemented in this work is

$$C_{\text{p}}^{\text{RVIF}}(t) = C_{\text{RV}}(t - t_{\text{RV}}) \otimes k_{\text{d}}\exp(-k_{\text{d}}t), \quad \text{Eq. 4}$$

where the time delay parameter $t_{\text{RV}}$ (s) denotes the time delay between the RV where the image-derived input function is extracted and the arrival of the radiotracer in the tissue of interest. The dispersion parameter $k_{\text{d}}$ (min$^{-1}$) aims to adaptively correct the dispersion effect between the 2 sites. The same $C_{\text{p}}^{\text{RVIF}}(t)$ (Eq. 4) is also used for $C_{\text{wb}}(t)$ in the RVIF model. The parameters $t_{\text{RV}}$ and $k_{\text{d}}$ are jointly estimated with other kinetic parameters during time–activity curve fitting.

On the other hand, an LV-derived input function (LVIF) is typically used for modeling lung tumors (30–32). The model supposes that the bronchial arteries, which are downstream from the LV, are the dominant blood supply of the tissue of interest. Similar to the RVIF model, the LVIF model (Fig. 1B) to be compared in this work is

$$C_{\text{p}}^{\text{LVIF}}(t) = C_{\text{LV}}(t - t_{\text{LV}}) \otimes k_{\text{d}}\exp(-k_{\text{d}}t), \quad \text{Eq. 5}$$
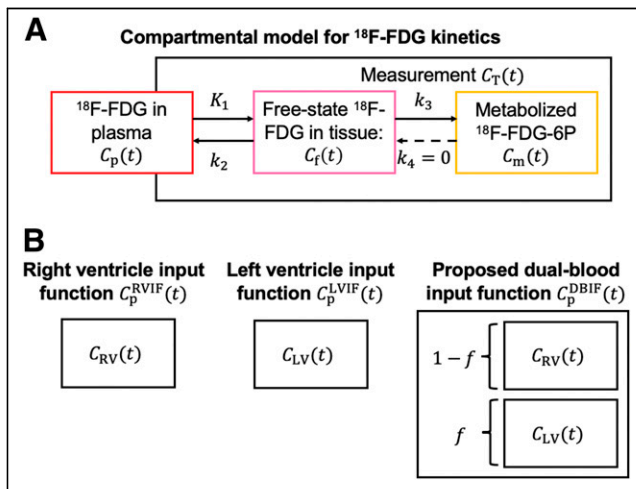
where $t_{\text{LV}}$ (s) denotes the time delay between the LV and the arrival of the radiotracer in the tissue of interest, and $k_{\text{d}}$ (min$^{-1}$) is for the dispersion correction. $C_{\text{p}}^{\text{LVIF}}(t)$ in Equation 5 is also used for $C_{\text{wb}}(t)$ in the LVIF model.

## Proposed DBIF

In this work, we hypothesized that the contribution of each blood supply is nonnegligible and should be accounted for when analyzing HTR dynamic PET data; hence, we proposed modeling both supplies rather than omitting either of them. The proposed DBIF is a linear combination of the 2 image-derived input functions $C_{\text{RV}}(t)$ and $C_{\text{LV}}(t)$ (Fig. 1B):

$$C_{\text{p}}^{\text{DBIF}}(t) = [fC_{\text{LV}}(t - t_{\text{LV}}) + (1 - f)C_{\text{RV}}(t - t_{\text{RV}})] \otimes k_{\text{d}}\exp(-k_{\text{d}}t),$$

Eq. 6

where $f$ represents the fractional contribution from the bronchial blood supply. As in the RVIF and LVIF models, $t_{\text{LV}}$ and $t_{\text{RV}}$ are the time delays for each of the 2 blood supplies and $k_{\text{d}}$ is the dispersion parameter. This

setting of 2 separate time-delay parameters and 1 comprehensive dispersion parameter was selected on the basis of our initial studies of curve fitting and parameter quantification. Similar to the single-input models, $C_{wb}(t)$ is modeled by $C_p^{DBIF}(t)$ in the DBIF model. Again, all parameters are jointly estimated with other kinetic parameters through time–activity curve fitting. The DBIF model is equivalent to the RVIF model if $f = 0$ and the LVIF model if $f = 1$.

With this DBIF model, a tissue time–activity curve $C_T(t)$ can be decomposed into an LV-supplied component $C_T^{LV}(t)$ and an RV-supplied component $C_T^{RV}(t)$:

$$C_T(t) = C_T^{LV}(t) + C_T^{RV}(t), \qquad \text{Eq. 7}$$

where the decomposed time–activity curves are calculated by

$$C_T^{LV}(t) = f\Big((1-v_b)H(t;\kappa) \otimes C_p^{LVIF}(t) + v_b C_p^{LVIF}(t)\Big), \qquad \text{Eq. 8}$$

$$C_T^{RV}(t) = (1-f)\Big((1-v_b)H(t;\kappa) \otimes C_p^{RVIF}(t) + v_b C_p^{RVIF}(t)\Big), \qquad \text{Eq. 9}$$

with $C_p^{LVIF}(t)$ and $C_p^{RVIF}(t)$ given by Equations 5 and 4, respectively.

### Evaluation of Statistical Fit Quality

To assess the statistical fitting quality of the 3 models (RVIF, LVIF, and DBIF), the corrected Akaike information criterion (AICc) was used (33,34):

$$\text{AICc} = M \ln\left(\frac{\text{WRSS}}{M}\right) + 2N + \frac{2N^2 + 2N}{M-N-1}, \qquad \text{Eq. 10}$$

in which $N$ is the number of unknown parameters ($N = 6$, 6, and 8 for the LVIF, RVIF, and DBIF models, respectively). The AICc considers the correction to the limited sample size $\frac{M}{n} \le 40$ (35) and is a balance between the goodness of curve fitting and model simplicity. A lower AICc value indicates better fitting quality. AICc values of the 3 models (LVIF, RVIF, and DBIF) were compared to quantify any improvement in fitting quality by the proposed DBIF model.

### Impact on Kinetic Quantification

The impact of the DBIF model was evaluated in relation to the quantification of kinetic parameters of major interest by comparing the results with those derived from the single-blood input function models. The investigated parameters included $^{18}$F-FDG delivery rate $K_1$, $^{18}$F-FDG net influx rate $K_i = K_1 k_3/(k_2 + k_3)$, fractional blood volume $v_b$, and time delay parameters $t_{LV}$ and $t_{RV}$. The LV fraction $f$, uniquely estimated by the DBIF model, was also investigated. Further, we compared the statistical difference between the lung tissue group and the lung tumor group using the Mann–Whitney $U$ test of the kinetic parameters quantified by different models. A $P$ value of less than 0.05 was considered to be significant.

### Demonstration of Multiparametric Imaging Using the DBIF Model

In addition to the ROI-based analysis, we applied the proposed DBIF model for voxel-wise parametric imaging to acquire multiparametric images of lung $K_1$, $K_i$, $v_b$, and $f$. Kernel smoothing was applied to the dynamic images to reduce noise (28).

As shown by Equation 7, one property of the DBIF model is to separate the LV-supplied and RV-supplied components. Therefore, we also used the decomposition to generate dynamic lung activity images showing the supply by the individual LVIF and RVIF.

## RESULTS

### HTR Dynamic Images of Subjects with Lung Tumors

Figure 2A shows the HTR total-body dynamic images of a representative cancer subject with lung metastasis in maximum-intensity projections, and Figure 2B shows the corresponding ROI time–activity curves extracted from the images. After the intravenous administration at around 10 s, the tracer traveled through the RV (Fig. 2A, 17–18 s) and arrived at the lungs (Fig. 2A, 22–23 s) through the pulmonary arteries. The tracer then flowed into the LV (Fig. 2A, 27–28 s) through the pulmonary vein. Hence, the arrival order of the early-phase time–activity curve peak is RV (at ∼17 s), lung tissue (at ∼22 s), and LV (at ∼27 s), as seen in Figure 2B. However, the lung tumor time–activity curve had a first peak at about 20 s (∼3 s after the RV peak) and a second peak at about 32 s (∼5 s after the LV peak, also visible in Fig. 2A), and the latter is later than the LV peak. This observation suggests a dual-blood-supply effect in the lung tumor.

### Time–Activity Curve Fitting Using Different Input Function Models

Figure 3A and Supplemental Figure 2 show examples of fitting the time–activity curves of a lung tumor from a cancer subject and a normal lung tissue sample from a healthy subject by the 2 single-input models (RVIF and LVIF) and the DBIF model. For the tumor time–activity curve, neither the RVIF nor the LVIF model was able to fit the 2 peaks in the early phase. However, the DBIF model achieved better fitting. The nontumor lung tissue time–activity curve fitting by the LVIF model was poor, whereas the RVIF and DBIF had similar good results. The time–activity curve fitting quality is further evaluated by AICc in Table 1 and Figure 3B. For the normal lung tissue from healthy subjects and the nontumor lung tissue from cancer subjects, the AICc of the RVIF model was much lower than the LVIF model, confirming the appropriateness of using RVIF for modeling lung tissue. Compared with RVIF and the LVIF, the DBIF model achieved the best AICc, especially for the modeling of lung tumor time–activity curves.
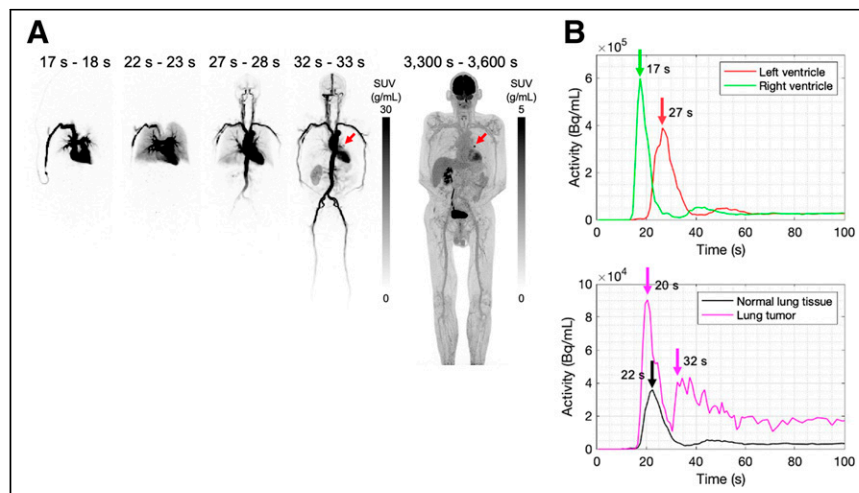


**FIGURE 2.** Cancer subject with lung metastasis. (A) HTR total-body $^{18}$F-FDG dynamic images acquired with uEXPLORER PET/CT system. Arrows point to lesion. (B) HTR time–activity curves extracted from dynamic image set. Nontumor lung tissue time–activity curve is averaged from 5 ROIs placed in 5 lung lobes, and lung tumor time–activity curve is obtained as shown in Supplemental Figure 1B.
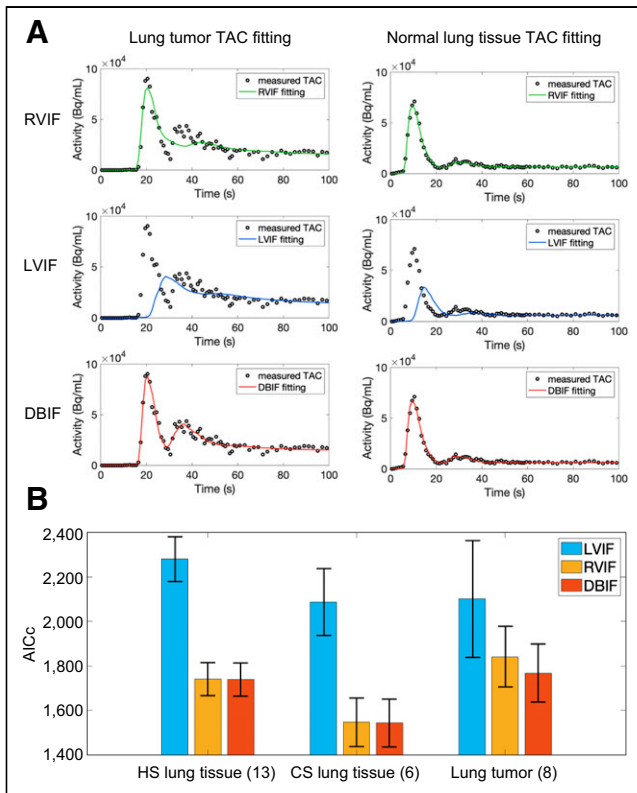
FIGURE 3. (A) HTR time–activity curve fitting of lung metastasis from genitourinary cancer subject and normal lung tissue from healthy subject with 3 models: RVIF, LVIF, and DBIF. (B) AICc of RVIF, LVIF models, and proposed DBIF model in lung tissue groups and lung tumor group. Lower values indicate better fitting quality. CS = cancer subject; HS = healthy subject.

For an illustrative example, the time–activity curves of the lung tissue and the lung tumor (Fig. 3A) were further decomposed in Figure 4 according to the individual LV and RV blood supplies using Equation 7. In the normal lung tissue, the LV-supplied component was small, with $f = 0.045$. In comparison, for the tumor time–activity curve, the LV-supplied component contributed significantly to fitting the second peak ($\sim35$ s), with $f = 0.31$.

### Statistical Analysis of Estimated *f* in Lung Tissue and Tumors

Figure 5A compares the LV fraction $f$ of the DBIF model in the lung tissue of healthy subjects, lung tissue of cancer subjects,

### TABLE 1
AICc Value of Time–Activity Curve Fitting of Normal Lung Tissue of Healthy Subjects, Lung Tissue of Cancer Subjects, and Lung Tumors by Kinetic Models with Different Input Functions

| | AICc | | |
|---|---|---|---|
| Model | Normal lung tissue of healthy subjects ($n = 13$) | Lung tissue of cancer subjects ($n = 6$) | Lung tumors of cancer subjects ($n = 8$) |
| LVIF | $2,280.4 \pm 101.1$ | $2,087.0 \pm 150.9$ | $2,101.6 \pm 262.5$ |
| RVIF | $1,741.0 \pm 74.7$ | $1,546.1 \pm 109.5$ | $1,841.6 \pm 135.6$ |
| DBIF | $1,739.1 \pm 75.1$ | $1,542.8 \pm 108.0$ | $1,767.5 \pm 130.1$ |
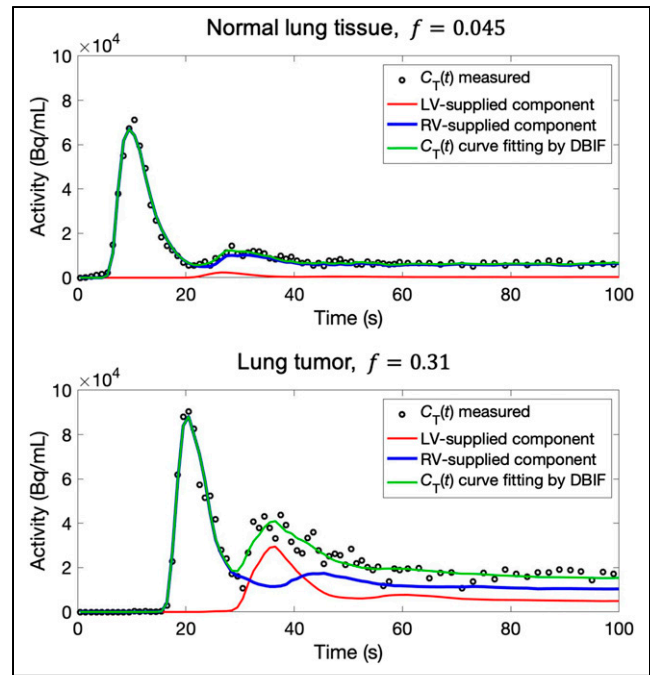


FIGURE 4. Examples of decomposition of fitted time–activity curve into LV-supplied component and RV-supplied component in DBIF model for normal lung tissue time–activity curve from healthy subject and lung tumor time–activity curve from cancer subject.

and lung tumors. The estimations of $f$ by DBIF for the 3 groups were $0.037 \pm 0.013$, $0.041 \pm 0.027$, and $0.30 \pm 0.27$, respectively. The primary tumors had $f = 0.35 \pm 0.45$, whereas metastases had $f = 0.27 \pm 0.16$. The $U$ tests indicated significant differences between the tumor group and the other 2 lung tissue groups (tumors vs. lung tissue of healthy subjects, $P < 0.0003$; tumors vs. lung tissue of cancer subjects, $P < 0.003$). No statistical difference was observed between the healthy-subject lung tissue and cancer-subject lung tissue ($P > 0.4$). The characteristics and the $f$ quantification of each lung tissue sample and tumor are listed in Supplemental Table 1.

### Impact of DBIF on Kinetic Quantification

The difference in $f$ led to changes in the estimation of kinetic parameters of interest. The impact on the normal lung tissue of healthy subjects and lung tumors is shown in Table 2, and the kinetic quantification of nontumor lung tissue of cancer subjects is shown in Supplemental Table 2. Compared with the 2 single-input models (RVIF and LVIF), the DBIF resulted in higher $v_b$ and lower $K_1$ in both normal lung tissue and lung tumors. Particularly, the $v_b$ estimated by DBIF for lung tissue of healthy subjects was closer to the reference value of 0.16 as reported in the literature (*27*).

Figures 5B and 5C further compare $K_1$ and $K_i$ of the DBIF model for differentiating lung tumors from normal lung tissue of healthy subjects or nontumor lung tissue of cancer subjects. Both kinetic parameters showed a statistical group difference ($P < 0.01$). The comparisons between the lung tissue and tumors using the DBIF and single-input models are summarized in Table 2 (tumors vs. healthy-subject lung tissue) and Supplemental Table 2 (tumors vs. cancer-subject nontumor lung tissue). The RVIF model had worse performance than DBIF and LVIF for using $K_1$ to differentiate lung tumors, whereas the LVIF model had less
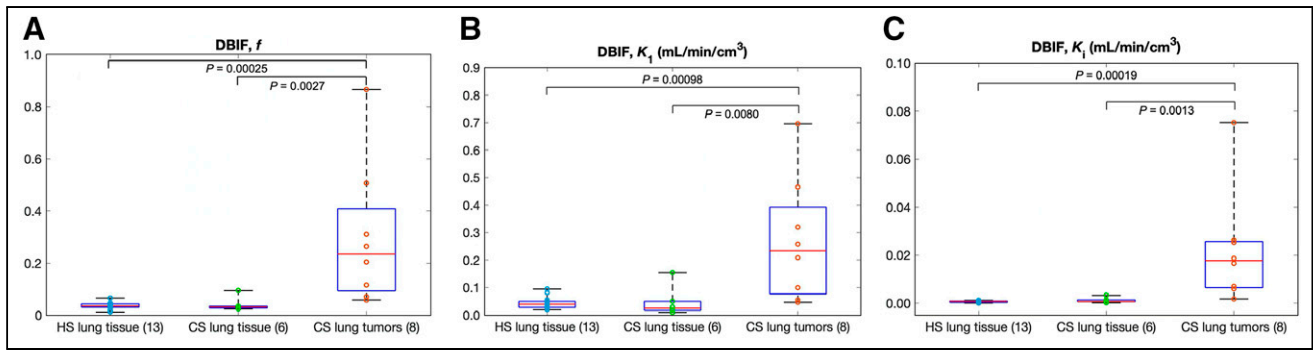
**FIGURE 5.** Comparison of lung tissue (from healthy subjects and cancer subjects) and lung tumors using kinetic parameters estimated by proposed DBIF model: LV fraction $f$ (A), $^{18}$F-FDG delivery rate $K_1$ (B), and $^{18}$F-FDG net influx rate $K_i$ (C). $P$ values are for Mann–Whitney $U$ test. CS = cancer subject; HS = healthy subject.

power than DBIF and RVIF for using $K_i$ to differentiate tumors, as indicated by the $P$ values. In addition, $t_{RV}$ and $t_{LV}$ by the DBIF tended to be different between lung tissue and lung tumors, as shown in Table 2. Overall, the DBIF demonstrated a more robust differentiation performance.

### Demonstration of Multiparametric Imaging

Figure 6 shows the parametric images ($f$, $K_1$, $K_i$, and $v_b$) of the total lung of a cancer subject by the DBIF model as compared with the image of the SUV. The parametric images show a clear difference in the lung tumors and surrounding tissue in $f$, $K_1$, and $K_i$, supporting the ROI-based analysis.

Figure 7 shows the decomposition of the dynamic images into the LV-supplied and RV-supplied components for 1 subject. When the tracer first passed through the lung via the pulmonary artery at 20–22 s, the measured activity was all in the RV-supplied component, and there was no LV-related component. However,

when the second peak of the tumor time–activity curve appeared at 32–34 s, the LV-supplied component appeared in the tumors and was the dominant contribution to the total measured activity in those tumors. The LV-supplied component continued to contribute to the total activity until the late phase of the 1-h scan.

### DISCUSSION

In this study, we investigated DBIF in normal lung tissue and lung tumors using HTR dynamic $^{18}$F-FDG imaging enabled with a total-body PET scanner. To the best of our knowledge, this was the first time that the dual blood supply of the lung tumor was monitored using dynamic PET and modeled by kinetic modeling. It is also worth noting that the DBIF model is not limited to dynamic $^{18}$F-FDG PET but also can be used for lung studies with other tracers (e.g., perfusion tracers such as $H_2^{15}O$ or $^{11}C$-butanol) (36). Compared with previous dynamic CT studies of lung dual

**TABLE 2**
Comparison of Normal Lung Tissue of Healthy Subjects with Lung Tumors Using $^{18}$F-FDG $K_1$, $v_b$, $K_i$, $t_{LV}$, and $t_{RV}$ Estimated by Kinetic Models with Different Input Functions

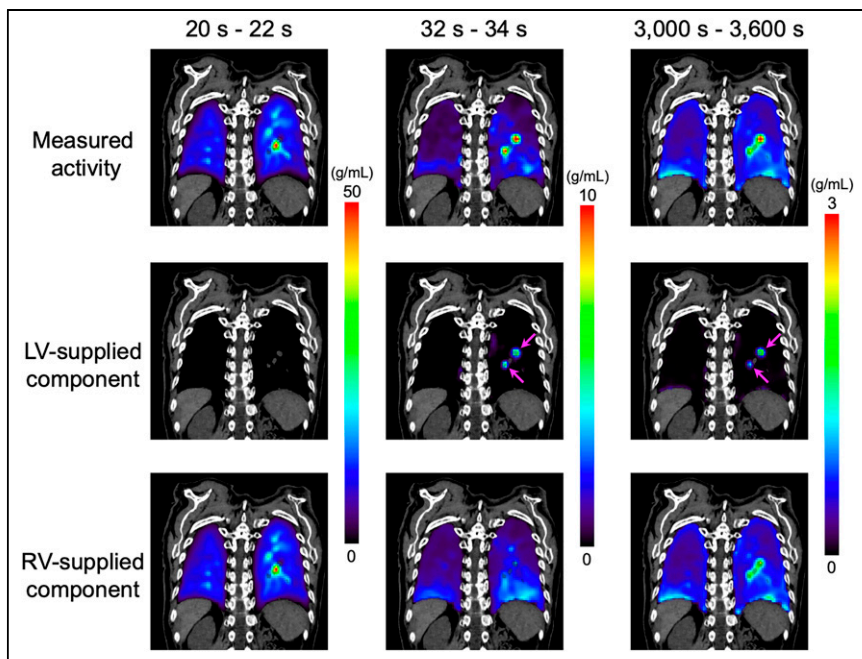| Parameter | Model | Lung tissue ($n = 13$) | Lung tumor ($n = 8$) | $P$ |
|---|---|---|---|---|
| $K_1$ (mL/min/cm$^3$) | RVIF | 0.066 ± 0.030 | 0.33 ± 0.33 | 0.013 |
| | LVIF | 0.053 ± 0.028 | 0.42 ± 0.37 | 0.00034 |
| | DBIF | 0.044 ± 0.022 | 0.27 ± 0.22 | 0.00098 |
| $v_b$ | RVIF | 0.14 ± 0.03 | 0.18 ± 0.10 | 0.86 |
| | LVIF | 0.10 ± 0.03 | 0.14 ± 0.12 | 0.74 |
| | DBIF | 0.15 ± 0.03 | 0.21 ± 0.10 | 0.23 |
| $K_i$ (mL/min/cm$^3$) | RVIF | 0.00076 ± 0.00047 | 0.022 ± 0.024 | 0.00019 |
| | LVIF | 0.00007 ± 0.00014 | 0.020 ± 0.024 | 0.00098 |
| | DBIF | 0.00061 ± 0.00034 | 0.022 ± 0.023 | 0.00019 |
| $t_{RV}$ (s) | RVIF | 2.16 ± 0.38 | 2.3 ± 3.3 | 0.14 |
| | LVIF | — | — | — |
| | DBIF | 2.17 ± 0.35 | 1.3 ± 0.9 | 0.039 |
| $t_{LV}$ (s) | RVIF | — | — | — |
| | LVIF | 0 ± 0 | 0.4 ± 1.1 | 0.24 |
| | DBIF | 13.0 ± 3.0 | 5.5 ± 5.7 | 0.0042 |

$P$ values are for Mann–Whitney $U$ test.
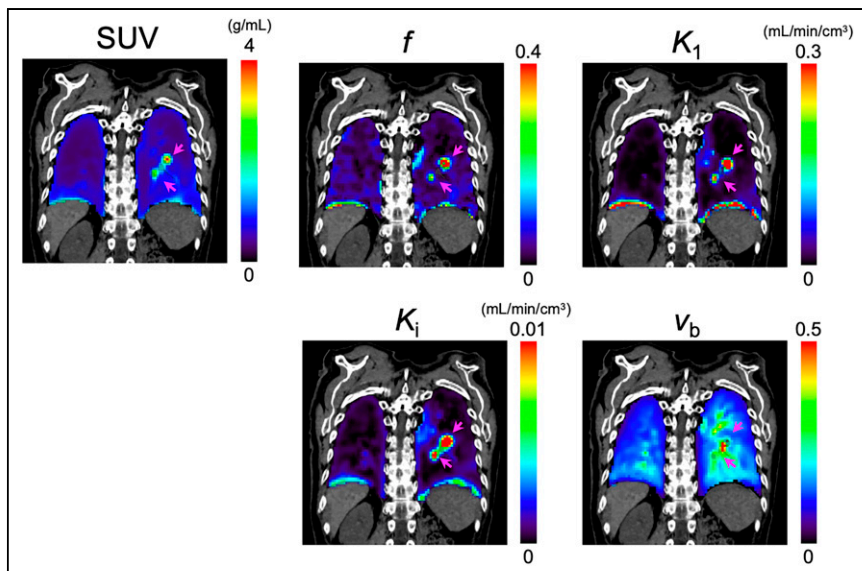
**FIGURE 6.** Comparison of total-lung $^{18}$F-FDG SUV image and parametric images for cancer subject with 2 metastatic lung nodules (arrows). Parametric images include LV fraction $f$, $^{18}$F-FDG delivery rate $K_1$, $^{18}$F-FDG net influx rate $K_i$, and fractional blood volume $v_b$ generated by proposed DBIF model. Coronal PET images are overlaid on corresponding CT slice.

blood supply (8–11) that were limited to a short axial field of view, our total-body PET study covered the total lung and enabled a multiparametric quantification of tracer kinetics, especially $f$, $K_1$, and $K_i$.

The significance of DBIF was demonstrated for HTR lung kinetic modeling by comparing the DBIF model with single-input models (i.e., LVIF and RVIF). The DBIF model achieved the best AICc for time–activity curve fitting, especially for tumor time–activity curves, whereas the LVIF and the RVIF were not able to



**FIGURE 7.** Dynamic $^{18}$F-FDG images of cancer subject with lung metastases (top) were decomposed into LV-supplied component and RV-supplied component using DBIF model. $^{18}$F-FDG PET images are overlaid on corresponding CT slice, and arrows point at metastases.

provide good fitting (Fig. 3). A further test of time–activity curve fitting (Supplemental Table 3) found that the DBIF model still achieved the best fitting when a different nonuniform weighting scheme was used (37). However, the efficacy of the DBIF model was compromised for data with a lower temporal resolution (e.g., 10 s/frame; Supplemental Table 4), indicating the importance of the HTR data for the application of DBIF.

The DBIF model had a significant impact on kinetic parameter quantification, particularly for $^{18}$F-FDG delivery rate $K_1$ and fractional blood volume $v_b$ (Table 2). More notably, the DBIF model also provides an estimation of the fraction of the bronchial supply (i.e., $f$) and the fraction of pulmonary supply (i.e., $1-f$), which were significantly different in lung tumors and lung tissue (Fig. 5A). In addition, $f$ also has the potential to be estimated with a shortened dynamic scan duration, for example, 0–2 min, as suggested by the preliminary results shown in Supplemental Table 5, though a more comprehensive study is warranted. The quantification of $f$ may provide insights into the angiogenesis of lung tumors (9) to characterize lung nodules (10), which may have an application in evaluating malignancy from benign lesions to potentially address the high false-positive challenge resulting from low-dose CT lung cancer screening (24). Furthermore, the potential applications of $f$ are not limited to lung cancer but also may encompass other lung diseases, such as asthma (38), acute lung inflammation (3), and coronavirus disease 2019 (39). For example, bronchial circulation is altered in asthma, and $f$ thus has the potential to be used for evaluating treatment efficacy (40,41).

In the proposed DBIF model, the same dispersion parameter $k_d$ was used to account for the dispersion effects in both blood supplies. This choice was based on its comparison with multiple other options, including no dispersion correction, dispersion correction for the LVIF only, dispersion correction for the RVIF only, and 2 different dispersion corrections for the LVIF and RVIF. The shared dispersion correction provided the most robust and physiologically reasonable results in the comparison (results not shown). It is also worth noting that the lung DBIF model proposed in this study is mathematically and physiologically different from the DBIF model used for liver PET studies (42,43) that consider the dual blood supplies from the hepatic artery and portal vein.

This work has some limitations. Primary lung tumors and lung metastases were pooled together for statistical analysis because of the limited sample size. It is possible that the dual-blood input effect was different in primary lung cancer

$(f = 0.35 \pm 0.45)$ and lung metastases $(f = 0.27 \pm 0.16)$, but further analysis was limited because of a small sample size. It would be valuable to further subtype the tumor group in future investigations. The proposed DBIF model is more complex and involves 2 more parameters ($f$ and an additional time delay parameter) than the single-blood input function models. We also tested using a single time delay for both LVIF and RVIF in the DBIF model. However, the result suggested the need for different time delays for the 2 input functions. Although the new model has increased complexity, its benefits were demonstrated by time–activity curve fitting quality and the impact on the quantification of kinetic parameters of interest. Our future work will further explore the potential of these kinetic parameters (e.g., $K_1$ and $f$) as disease biomarkers. Also, the fact that the air fraction correction (*44,45*) was not included in this study may have impacted the quantitative values of $K_1$ and $K_i$. Our future work will also investigate this direction.

## CONCLUSION

The effect of modeling lung dual blood supply was demonstrated using HTR dynamic total-body PET. The proposed DBIF model improved time–activity curve fitting quality, enabled quantification of the vascular fraction parameter $f$, and led to a nonnegligible impact on quantification of other kinetic parameters (e.g., $v_b$ and $K_1$). The DBIF effect was higher in lung tumors than in lung tissue. HTR dynamic imaging with total-body PET has the potential to be a sensitive tool for investigating lung physiology and diseases.

## DISCLOSURE

## ACKNOWLEDGMENTS

### KEY POINTS

**QUESTION:** Can the DBIF that accounts for the dual blood supply of the lungs improve kinetic modeling of the lung tissue and lung tumors in HTR dynamic imaging with total-body PET?

**PERTINENT FINDINGS:** The DBIF model achieved improved time–activity curve fitting compared with single-blood input function models and led to quantification of the vascular fraction parameter. The effect of dual-blood-supply modeling was larger in lung tumors than in lung tissue as indicated by this kinetic parameter.

**IMPLICATIONS FOR PATIENT CARE:** The incorporation of the DBIF in HTR dynamic PET imaging of the lung may improve the diagnosis and evaluation of lung diseases.

## REFERENCES

1. West JB. Evolution of the pulmonary circulation and the right heart. In: Peacock AJ, Naeije R, Rubin LJ, eds. *Pulmonary Circulation: Diseases and Their Treatment.* CRC Press; 2016:22–30.
2. Suresh K, Shimoda LA. Lung circulation. In: Terjung R, ed. *Comprehensive Physiology.* Wiley; 2016:897–943.
3. Deffebach ME, Charan NB, Lakshminarayan S, Butler J. The bronchial circulation. *Am Rev Respir Dis.* 1987;135:463–481.
4. Walker CM, Rosado-de-Christenson ML, Martínez-Jiménez S, Kunin JR, Wible BC. Bronchial arteries: anatomy, function, hypertrophy, and anomalies. *Radiographics.* 2015;35:32–49.
5. McCullagh A, Rosenthal M, Wanner A, Hurtado A, Padley S, Bush A. The bronchial circulation: worth a closer look—a review of the relationship between the bronchial vasculature and airway inflammation. *Pediatr Pulmonol.* 2010;45:1–13.
6. Mitzner W, Lee W, Georgakopoulos D, Wagner E. Angiogenesis in the mouse lung. *Am J Pathol.* 2000;157:93–101.
7. Kiessling F, Boese J, Corvinus C, et al. Perfusion CT in patients with advanced bronchial carcinomas: a novel chance for characterization and treatment monitoring? *Eur Radiol.* 2004;14:1226–1233.
8. Yuan X, Zhang J, Ao G, Quan C, Tian Y, Li H. Lung cancer perfusion: can we measure pulmonary and bronchial circulation simultaneously? *Eur Radiol.* 2012; 22:1665–1671.
9. Nguyen-Kim TDL, Frauenfelder T, Strobel K, Veit-Haibach P, Huellner MW. Assessment of bronchial and pulmonary blood supply in non-small cell lung cancer subtypes using computed tomography perfusion. *Invest Radiol.* 2015;50:179–186.
10. Yuan X, Zhang J, Quan C, et al. Differentiation of malignant and benign pulmonary nodules with first-pass dual-input perfusion CT. *Eur Radiol.* 2013;23: 2469–2474.
11. Chen X, Xu Y, Duan J, Li C, Sun H, Wang W. Correlation of iodine uptake and perfusion parameters between dual-energy CT imaging and first-pass dual-input perfusion CT in lung cancer. *Medicine (Baltimore).* 2017;96:e7479.
12. Wang G, Rahmim A, Gunn RN. PET parametric imaging: past, present, and future. *IEEE Trans Radiat Plasma Med Sci.* 2020;4:663–675.
13. de Prost N, Costa EL, Wellman T, et al. Effects of surfactant depletion on regional pulmonary metabolic activity during mechanical ventilation. *J Appl Physiol.* 2011; 111:1249–1258.
14. Chen DL, Schuster DP. Positron emission tomography with [18F]fluorodeoxyglucose to evaluate neutrophil kinetics during acute lung injury. *Am J Physiol Lung Cell Mol Physiol.* 2004;286:L834–L840.
15. de Prost N, Tucci MR, Melo MFV. Assessment of lung inflammation with 18F-FDG PET during acute lung injury. *AJR.* 2010;195:292–300.
16. Chen DL, Mintun MA, Schuster DP. Comparison of methods to quantitate 18F-FDG uptake with PET during experimental acute lung injury. *J Nucl Med.* 2004;45:1583–1590.
17. Schroeder T, Vidal Melo MF, Musch G, Harris RS, Venegas JG, Winkler T. Image-derived input function for assessment of 18F-FDG uptake by the inflamed lung. *J Nucl Med.* 2007;48:1889–1896.
18. Cherry SR, Badawi RD, Karp JS, Moses WW, Price P, Jones T. Total-body imaging: transforming the role of positron emission tomography. *Sci Transl Med.* 2017; 9:eaaf6169.
19. Alberts I, Hünermund J-N, Prenosil G, et al. Clinical performance of long axial field of view PET/CT: a head-to-head intra-individual comparison of the Biograph Vision Quadra with the Biograph Vision PET/CT. *Eur J Nucl Med Mol Imaging.* 2021;48:2395–2404.
20. Pantel AR, Viswanath V, Daube-Witherspoon ME, et al. PennPET Explorer: human imaging on a whole-body imager. *J Nucl Med.* 2020;61:144–151.
21. Badawi RD, Shi H, Hu P, et al. First human imaging studies with the EXPLORER total-body PET scanner. *J Nucl Med.* 2019;60:299–303.
22. Zhang X, Cherry SR, Xie Z, Shi H, Badawi RD, Qi J. Subsecond total-body imaging using ultrasensitive positron emission tomography. *Proc Natl Acad Sci USA.* 2020;117:2265–2267.
23. Feng T, Zhao Y, Shi H, et al. Total-body quantitative parametric imaging of early kinetics of 18F-FDG. *J Nucl Med.* 2021;62:738–744.
24. Jonas DE, Reuland DS, Reddy SM, et al. Screening for lung cancer with low-dose computed tomography: updated evidence report and systematic review for the US preventive services task force. *JAMA.* 2021;325:971–987.
25. Spencer BA, Berg E, Schmall JP, et al. Performance evaluation of the uEXPLORER total-body PET/CT scanner based on NEMA NU 2-2018 with additional tests to characterize PET scanners with a long axial field of view. *J Nucl Med.* 2021;62:861–870.

26. Cherry SR, Sorenson JA, Phelps ME. Tracer kinetic modeling. In: *Physics in Nuclear Medicine.* 4th ed. Saunders; 2012:379–405.

27. Chen DL, Cheriyan J, Chilvers ER, et al. Quantification of lung PET images: challenges and opportunities. *J Nucl Med.* 2017;58:201–207.

28. Wang G, Nardo L, Parikh M, et al. Total-body PET multiparametric imaging of cancer using a voxel-wise strategy of compartmental modeling. *J Nucl Med.* 2022; 63:1274–1281.

29. Wang Y, Spencer BA, Schmall J, et al. High-temporal-resolution lung kinetic modeling using total-body dynamic PET with time-delay and dispersion corrections. *J Nucl Med.* 2023;64:1154–1161.

30. Torizuka T, Nobezawa S, Momiki S, et al. Short dynamic FDG-PET imaging protocol for patients with lung cancer. *Eur J Nucl Med.* 2000;27:1538–1542.

31. Dimitrakopoulou-Strauss A, Georgoulias V, Eisenhut M, et al. Quantitative assessment of SSTR2 expression in patients with non-small cell lung cancer using $^{68}$Ga-DOTATOC PET and comparison with $^{18}$F-FDG PET. *Eur J Nucl Med Mol Imaging.* 2006;33:823–830.

32. Karakatsanis NA, Lodge MA, Zhou Y, Wahl RL, Rahmim A. Dynamic whole-body PET parametric imaging: II. Task-oriented statistical estimation. *Phys Med Biol.* 2013;58:7419–7445.

33. Akaike H. A new look at the statistical model identification. *IEEE Trans Automat Contr.* 1974;19:716–723.

34. Glatting G, Kletting P, Reske SN, Hohl K, Ring C. Choosing the optimal fit function: comparison of the Akaike information criterion and the F-test—choosing the optimal fit function. *Med Phys.* 2007;34:4285–4292.

35. Richard MA, Fouquet JP, Lebel R, Lepage M. Determination of an optimal pharmacokinetic model of $^{18}$F-FET for quantitative applications in rat brain tumors. *J Nucl Med.* 2017;58:1278–1284.

36. Li EJ, López JE, Spencer BA, et al. Total-body perfusion imaging with [$^{11}$C]-butanol. *J Nucl Med.* 2023;64:1831–1838.

37. Thiele F, Buchert R. Evaluation of non-uniform weighting in non-linear regression for pharmacokinetic neuroreceptor modelling. *Nucl Med Commun.* 2008;29:179–188.

38. Jeffery PK. Remodeling in asthma and chronic obstructive lung disease. *Am J Respir Crit Care Med.* 2001;164:S28–S38.

39. Ackermann M, Tafforeau P, Wagner WL, et al. The bronchial circulation in COVID-19 pneumonia. *Am J Respir Crit Care Med.* 2022;205:121–125.

40. Paredi P, Kharitonov SA, Barnes PJ. Correlation of exhaled breath temperature with bronchial blood flow in asthma. *Respir Res.* 2005;6:15.

41. Paredi P, Barnes PJ. The airway vasculature: recent advances and clinical implications. *Thorax.* 2009;64:444–450.

42. Keiding S. Bringing physiology into PET of the liver. *J Nucl Med.* 2012;53: 425–433.

43. Wang G, Corwin MT, Olson KA, Badawi RD, Sarkar S. Dynamic PET of human liver inflammation: impact of kinetic modeling with optimization-derived dual-blood input function. *Phys Med Biol.* 2018;63:155004.

44. Coello C, Fisk M, Mohan D, et al. Quantitative analysis of dynamic $^{18}$F-FDG PET/CT for measurement of lung inflammation. *EJNMMI Res.* 2017;7:47.

45. Holman BF, Cuplov V, Millner L, et al. Improved correction for the tissue fraction effect in lung PET/CT imaging. *Phys Med Biol.* 2015;60:7387–7402.